Nanoscale Advances

ROYAL SOCIETY OF CHEMISTRY

PAPER

View Article Online
View Journal | View Issue

Cite this: *Nanoscale Adv.*, 2022, **4**, 408

Effect of different molecular coatings on the heating properties of maghemite nanoparticles†

Marco Sanna Angotzi, ‡[ab] Valentina Mameli, ‡[ab] Shankar Khanal,[c] Miroslav Veverka,[c] Jana Vejpravova *[c] and Carla Cannas *[ab]

Received 24th June 2021
Accepted 8th November 2021

DOI: 10.1039/d1na00478f

rsc.li/nanoscale-advances

In this work, the effect of different molecular coatings on the alternating magnetic field-induced heating properties of 15 nm maghemite nanoparticles (NPs) in water dispersions was studied at different frequencies (159–782 kHz) and field amplitudes (100–400 G). The original hydrophobic oleate coating was replaced with dimercaptosuccinic acid (DMSA) or polyethylene glycol trimethoxysilane (PEGTMS), while cetrimonium bromide (CTAB) or stearic acid-poloxamer 188 (SA-P188) was intercalated or encapsulated, respectively, to transfer the dispersions into water. Surface modification, based on intercalation processes, induced clustering phenomena with the formation of spherical-like assemblies (CTAB and SA-P188), while ligand-exchange strategies kept the particles isolated. The clustering phenomenon has detrimental effects on the heating performances compared with isolated systems, in line with the reduction of Brown relaxation times. Furthermore, broader comprehension of the heating phenomenon in this dynamic system is obtained by following the evolution of SPA and ILP with time and temperature beyond the initial stage.

Introduction

Spinel ferrite nanoparticles (NPs), thanks to the excellent control of magnetic properties through chemical manipulation, represent ideal systems for many fields, such as environmental applications[1–5] and biomedicine.[6–8] In particular, their ability to release heat when subjected to an alternating magnetic field (*i.e.*, magnetic heat generation) makes them appealing for catalysis[9–12] and magnetic fluid hyperthermia (MFH).[13–15] When NPs are in the superparamagnetic (SPM) state, according to linear-response theory (LRT),[16] heat is released through relaxation losses, which can be associated with vector magnetization reversal inside the particle (Néel relaxation time, τ_N, eqn (1)), and through physical rotation of the particle in a fluid (Brown relaxation time, τ_B, eqn (2)):

$$\tau_N = \tau_0 e^{\frac{KV}{k_B T}} \quad (1)$$

$$\tau_B = \frac{3\eta V_H}{k_B T} \quad (2)$$

where τ_0 is the characteristic relaxation time (10^{-9} to 10^{-11} s),[17] K the anisotropy constant, V the inorganic volume of the particle, k_B the Boltzmann constant, T the temperature of the system, η the viscosity of the medium, and V_H the hydrodynamic volume of the particle. Therefore, the effective relaxation time (τ) accounts for both Néel and Brown mechanisms and is defined by:

$$\frac{1}{\tau} = \frac{1}{\tau_N} + \frac{1}{\tau_B} \quad (3)$$

which means that the faster relaxation time dominates the other one. For instance, considering magnetite NPs ($K = 3 \times 10^4$ J m^{-3}), the Néel relaxation is the dominant mechanism up to 15 nm, while beyond 20 nm, the Brown one prevails. Within the validity of LRT, the specific power absorption (SPA, or specific loss power SLP or specific absorption rate SAR) is related to the loss power density by the mass density of the particles (SPA $= P/\rho$), where P is defined as:

$$P = \frac{\mu_0^2 M_s^2 V H_0^2}{3 k_B T \tau} \frac{(2\pi f \tau)^2}{1 + (2\pi f \tau)^2} \quad (4)$$

where μ_0 is the vacuum permeability, M_s the saturation magnetization, V the particle volume, H_0 the applied field, k_B the Boltzmann constant, T the temperature, and f the applied frequency.

Other mechanisms responsible for the heat release are hysteresis losses, typical of multi-domain or blocked single-domain nanoparticles, which are associated with hysteretic

[a]*Department of Chemical and Geological Sciences, University of Cagliari, S.S. 554 Bivio per Sestu, Monserrato, 09042 CA, Italy. E-mail: ccannas@unica.it*

[b]*Consorzio Interuniversitario Nazionale per la Scienza e Tecnologia dei Materiali (INSTM), Via Giuseppe Giusti 9, 50121 Firenze (FI), Italy*

[c]*Department of Condensed Matter Physics, Charles University, Ke Karlovu 5, 12116 Prague 2, Czech Republic. E-mail: jana@mag.mff.cuni.cz*

† Electronic supplementary information (ESI) available: TGA analyses; magnetic measurements; MFH measurements; literature comparison. See DOI: 10.1039/d1na00478f

‡ These authors contributed equally to this work.

magnetic responses. For these systems, the power per unit of volume is given by the product of the frequency f and the hysteresis loop area $\mu_0 \oint H dM$. Besides this common distinction between hysteresis and relaxation losses, other authors have highlighted that in real systems both types might occur at the same time, especially if they are nearby the transition region between the SPM and the ferromagnetic regimes.[18]

Nevertheless, when dealing with colloidal dispersions, NPs tend to form clusters (aggregates if the assembly is permanent or agglomerates if it is reversible), affecting their Brownian motion and, consequently, the heat response. In the literature, only a few studies have been devoted to the investigation of clustering effects, showing contradictory results in terms of improvement[19–23] or deterioration[23–27] of the heat response, which consequently is hardly predictable. Indeed, inter-particle interactions, predominantly of dipolar origin, can occur among the particles in the colloidal state. Thus, the magnetic response might be affected by the occurrence of the random orientation or the alignement of individual magnetic moments. Therefore, a systematic study on a suitable model system needs to be developed, where the interparticle interactions and their influence in the heat response can be disentangled, keeping a constant chemical composition, size, and shape of the original nanoparticles.

Therefore, it is of primary importance to employ a synthesis method that guarantees the NPs with a defined shape, high crystallinity, and low size dispersity for a unique magnetic response, but that also features repeatability and low environmental impact.[28] These advantages have been recently found in an oleate-based solvothermal method that has been set up for the synthesis of spinel ferrite NPs, in the form of single phases,[29,30] mixtures,[31,32] core–shells,[7,8,33] and silver–ferrite flower-like heterostructures.[34]

In addition, the modification of the nanoparticles' surface is fundamental to ensure good colloidal stability and modulate the interparticle distance through the formation of clusters. Therefore, several stabilizers have been proposed in the literature, such as bonding of hydrophilic molecules to the NPs' surface, such as dimercaptosuccinic acid (DMSA),[35–39] functionalized silanes,[40–42] and carboxylic acids,[37,43–46] encapsulation of NPs in polymers such as dextran,[47–49] polyethylene glycol (PEG),[50–52] polyacrylic acid,[53–56] biopolymers,[57–60] *etc.* (Table 1S†). Up to now, various methods have been developed for the clustering of primary NPs, exploiting a self-assembly mechanism as the result of the spontaneous control of the nanoentities that interplay through noncovalent interactions with the help of surfactants such as SDS[61] or poloxamers.[62]

In this work, the aqueous colloidal dispersions of maghemite NPs with a diameter of 15 nm, prepared by a solvothermal method, were obtained through NPs' surface modification with commonly used molecules and polymers. DMSA, 2-[methoxy(polyethyleneoxy)$_{6-9}$propyl] trimethoxysilane (PEGTMS), cetrimonium bromide (CTAB), and stearic acid (SA) combined with poloxamer 188 (P188) were employed to modify the NPs' surface through ligand-exchange, intercalation, or encapsulation procedures. The heat response of the NPs was studied as a function of the molecular coating, by varying the frequency and amplitude of the applied high-frequency magnetic field, and correlated with the magnetic and colloidal properties, paying attention to the role of cluster formation. Furthermore, the evolution of SPA and intrinsic loss power (ILP) with time and temperature was followed to better understand the heat release phenomenon also after the initial stage.

Experimental

Chemicals

Oleic acid (90%) and iron chloride tetrahydrate (98%) were purchased from Alpha Aesar. 1-Pentanol (≥99%), cetrimonium bromide (CTAB, 98%), chloroform (99.4%), dimercaptosuccinic acid (DMSA, 90%), ethanol (99.8%), iron nitrate nonahydrate (≥98%), *n*-hexane (≥97%), sodium hydroxide (98%), toluene (99.7%), and triethylamine (TEA, >99.5%) were purchased from Sigma Aldrich. Dimethyl sulfoxide (DMSO, ≥99.5%) was purchased from Sigma. Poloxamer 188 (P188) and sodium hydroxide (1 mol L^{-1}) were purchased from Panreac. 2-[Methoxy(polyethyleneoxy)$_{6-9}$propyl] trimethoxysilane (PEGTMS, 90%) was purchased from ABCR GmBH. Stearic acid (SA, 97%) was purchased from Acros Organics.

Methods

Synthesis of the hydrophobic maghemite NPs. The oleate-capped NPs were prepared through a seed-mediated growth method under solvothermal conditions, as described in previous work.[30] First, 10 nm NPs were prepared. 2 mmol of Fe^{II}–oleate and 1 mmol of Fe^{III}–oleate, 10 mL of 1-pentanol, 10 mL of toluene, and 5 mL of water were added into a Teflon liner. The liner-free space was flushed with nitrogen and enclosed in a stainless-steel autoclave (Berghof DAB-2), briefly shaken, and put vertically into a preheated oven (220 °C) for 10 hours. After the treatment, the particles were separated with a magnet and the supernatant was discarded. The particles were dispersed in 10 mL of hexane, and then sedimented by adding 10 mL of ethanol. The washing procedure was repeated twice. Finally, the particles were dispersed in 5 mL of hexane and subjected to 3 minutes of centrifugation at 3000 rpm to remove any unstable particles. 30 mg of the 10 nm NPs were dispersed in 10 mL of toluene and placed in a Teflon liner (seeds). 2 mmol of Fe^{II}–oleate, 10 mL of 1-pentanol, and 5 mL of water were added to the liner. The subsequent solvothermal treatment and washing steps were the same as for the 10 nm NPs. The seed-mediated solvothermal synthesis was repeated five times (on different 10 nm NP aliquots), and the products were joined to obtain enough particles for the subsequent steps. The sample was labeled Fe_Ole.

The hydrophobic (oleate-capped) nanoparticles (Fe_Ole) were converted into hydrophilic ones by ligand exchange with DMSA and PEGTMS and by intercalation of CTAB or SA followed by encapsulation in P188.

Ligand exchange with DMSA.[63] About 16 mg of NPs was dispersed in 78 mL of toluene, followed by the addition of 1.7 mL dimethyl sulfoxide (DMSO) solution containing 31 mg of DMSA. The mixture was sonicated for 5 minutes and mechanically stirred for 48 hours at room temperature. The precipitated NPs

were recovered with a magnet, washed with 5 mL of hexane and three times with 5 mL of ethanol, and then dispersed in 4 mL of distilled water. One drop of NaOH 1 M was added to the dispersion to increase the pH and stabilize the NPs.

Ligand exchange with PEGTMS.[64] About 16 mg of NPs were dispersed in 7.5 mL of toluene, and then 1.5 mL of PEGTMS, 7.5 mL of TEA, and 0.15 mL of water were added. The mixture was mechanically stirred for 24 hours. After the treatment, the NPs were magnetically collected and washed with 5 mL of hexane and three times with 5 mL of ethanol, and then dispersed in 4 mL of distilled water.

Intercalation with CTAB.[65] About 16 mg of NPs was dispersed with 1 mL of chloroform, which was slowly added under stirring to a 4 mL water solution of 0.1 g of CTAB. The dispersion was stirred for 1 hour at 30 °C, and then heated for another hour at 60 °C to form a limpid black-colored dispersion.

Intercalation with SA and encapsulation in P188 (ref. 62). About 16 mg of NPs were dispersed in 0.8 mL of toluene, and then 1.3 mg of SA was added, and the mixture was heated at 75 °C for 10 minutes to melt the stearic acid. After that, 4 mL of a water solution of 0.5% w/w P188 was added to the organic dispersion and sonicated for 45 minutes in a cold (~10 °C) ultrasonic bath. The resulting microemulsion was stirred at room temperature to let the toluene evaporate.

After each post-synthesis modification, the aqueous dispersion was centrifuged to remove any unstable particle and stored in a vial. The samples were labeled Fe_DMSA, Fe_PEG, Fe_CTAB, and Fe_SA-P188, based on the employed molecules.

Characterization

The dispersions' concentrations were determined by Inductively Coupled Plasma – Optical Emission Spectrometry (ICP–OES). 0.5 mL of aqueous dispersion was digested by adding 4 mL HNO_3 and stirring at ~50 °C for two hours. The solutions were allowed to cool down, filtered, and diluted by using 2% v/v HNO_3 solution. The ICP measurements were performed on an Agilent 5110 spectrometer by analyzing Fe at wavelengths 238.204 nm, 259.940 nm, and 261.187 nm, and the concentration was averaged.

The samples were characterized by powder X-ray diffraction (XRD) using a Seifert X3000, equipped with a Cu anode (Kα radiation with $\lambda = 1.5418$ Å). The calibration of the peak position and instrumental width was done using powdered LaB_6 from NIST. The refinement of the structural parameters[66] was performed by the Rietveld method using the software MAUD[67] and adopting recommended fitting procedures.[68] The CIF structure COD ID used for the refinement is 1010369.[69]

Transmission electron microscopy (TEM) images were obtained using a JEOL JEM 1400 Plus operating at 120 kV. The particle size distribution was obtained by measuring over 1000 particles with the aid of the software Pebbles, setting a spherical shape for the elaboration.[70] The weighted-mean particle diameter was calculated through the following equation:[71]

$$D_{\mathrm{TEM\_V}} = \frac{\sum n_i d_i^4}{\sum n_i d_i^3} \quad (5)$$

High-resolution TEM images were obtained through a JEOL JEM 2010 UHR equipped with a 794 slow-scan CCD camera.

Fourier Transform Infrared (FT-IR) spectra were recorded in the region from 400 to 4000 cm^{-1} by using a Bruker Equinox 55 spectrophotometer. Samples were measured as KBr pellets. Spectra were processed using OPUS software.

Thermogravimetric analysis (TGA) curves were obtained using a PerkinElmer STA 6000, in the 25–850 °C range, with a heating rate of 10 °C min^{-1} under a 40 mL min^{-1} O_2 flow.

Room temperature (RT) ^{57}Fe Mössbauer spectroscopy was performed on a Wissel spectrometer using a transmission arrangement and proportional detector LND-45431. α-Fe foil was used as a standard, and the fitting procedure was done by using the NORMOS program to determine the isomer shift, quadrupole splitting, hyperfine field, and full width at half maximum (FWHM) of the signals.

Dynamic light scattering (DLS) and electrophoretic light scattering (ELS) measurements were performed on colloidal dispersions through a Malvern Instrument Zetasizer Nano ZSP equipped with a He–Ne laser ($\lambda = 633$ nm and max 5 mW) and operated at a scattering angle of 173°. The Brown relaxation time was calculated from the hydrodynamic diameter calculated from the number size distribution ($D_{\mathrm{DLS\_N}}$) through eqn (2), considering a temperature of 30 °C and a solvent viscosity of 7.92×10^{-4} kg m^{-1} s^{-1}.

The magnetic characterization of the dispersions was performed using a SQUID magnetometer (MPMS7XL, Quantum Design). The temperature-dependent magnetization response was measured at 100 Oe using zero-field-cooled (ZFC) and field cooled (FC) protocols. The blocking temperatures (T_b) were calculated as the maximum of the derivative of the difference between the FC and ZFC magnetization curves. The anisotropy constants (K) were calculated through eqn (6):[72]

$$K = \frac{25 k_B T_B}{V} \quad (6)$$

where V is the particle volume calculated from $D_{\mathrm{TEM\_V}}$. The Néel relaxation times were calculated by using eqn (1), considering a temperature of 30 °C and τ_0 equal to 10^{-9} s.

The heat response of NPs was recorded using a D5 system (Nano-Biomagnetic) in the frequency range 159–782 kHz with different amplitudes of the alternating magnetic field (100–400 G). The concentration of NPs in water dispersion was fixed to 1.12 mg mL^{-1} for all samples. A fiber-optic probe, which allows recording temperature with high accuracy, was used to monitor the solvent temperature during the experiment. Both the field and the frequency-dependent heat response was recorded under adiabatic conditions. The SPA of the NPs' dispersions was evaluated using the formula:

$$\mathrm{SPA} = \frac{C\delta}{\phi}\frac{\mathrm{d}T}{\mathrm{d}t} \quad (7)$$

where C and δ are the specific heat capacity and density of solvent, respectively, and φ the weight concentration of NPs in the water dispersion.

Results and discussion

An iron oxide sample (Fe_Ole) was prepared through an oleate-based seed-mediated growth approach under solvothermal conditions and characterized from the structural and morphological points of view by XRD, TEM, HRTEM, and room temperature (RT) ^{57}Fe Mössbauer spectroscopy.

The XRD diffraction pattern of the Fe_Ole sample and the Rietveld refinement are reported in Fig. 1a. Only diffraction peaks corresponding to a nanostructured spinel iron oxide are visible. The cell parameter (a, 8.359(1) Å) suggests the presence of maghemite nanoparticles (maghemite: 8.3515 Å from PDF card 039-1346; magnetite: 8.3960 Å from PDF card: 019-0629). The crystallite size calculated from Rietveld refinement is equal to 16.6(5) nm.

TEM images reveal well-separated spherical NPs with a particle size of 14.7 nm (Fig. 1b and 2), in fair agreement with the size obtained from XRD. The particle size dispersity is low enough ($\sigma = 10\%$) to generate superlattices in the TEM grid as soon as the solvent evaporates (Fig. 1b). The HRTEM image (Fig. 1c) shows highly crystalline particles with no evidence of an amorphous part or heterojunctions, suggesting epitaxial coating of iron oxide around the pre-formed seeds. Inter-fringe distances and the associated Miller's indices confirmed the spinel ferrite structure.

RT ^{57}Fe Mössbauer spectroscopy was performed to obtain information on the iron state (Fe^{II}/Fe^{III}) and the magnetic properties of the spinel ferrite NPs (Fig. 1d).[1,30] The spectrum of the sample Fe_Ole was fitted by using two sextets due to the expectation of the blocked state for nanoparticles of this size (*i.e.*, around 15 nm).[30] The two sextets presented hyperfine field values of 45.5 and 39.6 T, corresponding to iron cations in the tetrahedral and octahedral sites of the spinel ferrite structure.[73] The isomer shift for both the sextets is in the range 0.33–0.34 mm s^{-1}, indicating the almost complete absence of Fe^{II}, whose values are around 0.6–0.7 mm s^{-1}.[74] Since Fe^{II}–oleate was used for the synthesis, oxidation toward Fe^{III} occurred, which is expected over time.[30] The presence of maghemite is in agreement with the XRD data.

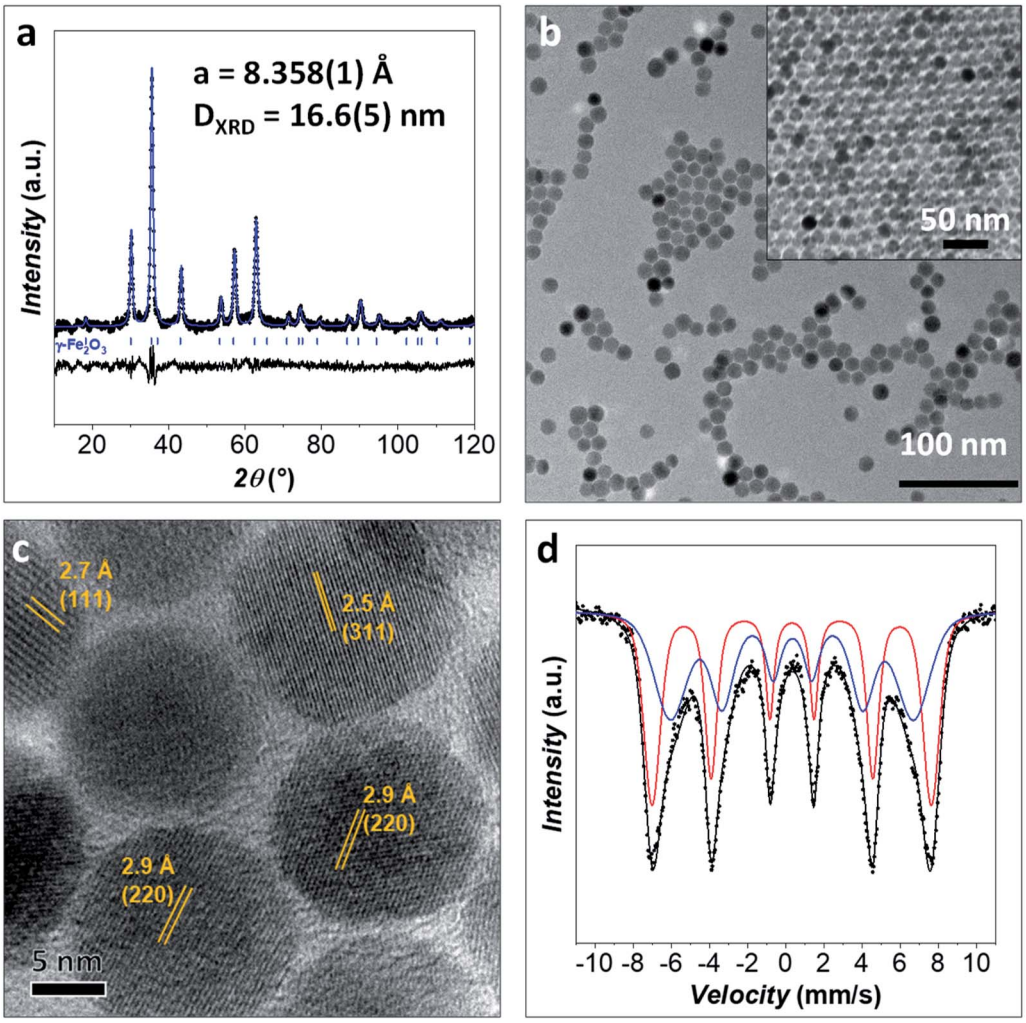

Fig. 1 Structural, magnetic, and morphological characterization of Fe_Ole: (a) Rietveld refinement of the XRD pattern; (b) TEM micrograph of the particles and superlattice assembly after solvent evaporation on a TEM grid (inset); (c) HRTEM image with inter-fringe distances and Miller's indices; (d) RT ^{57}Fe Mössbauer spectrum.

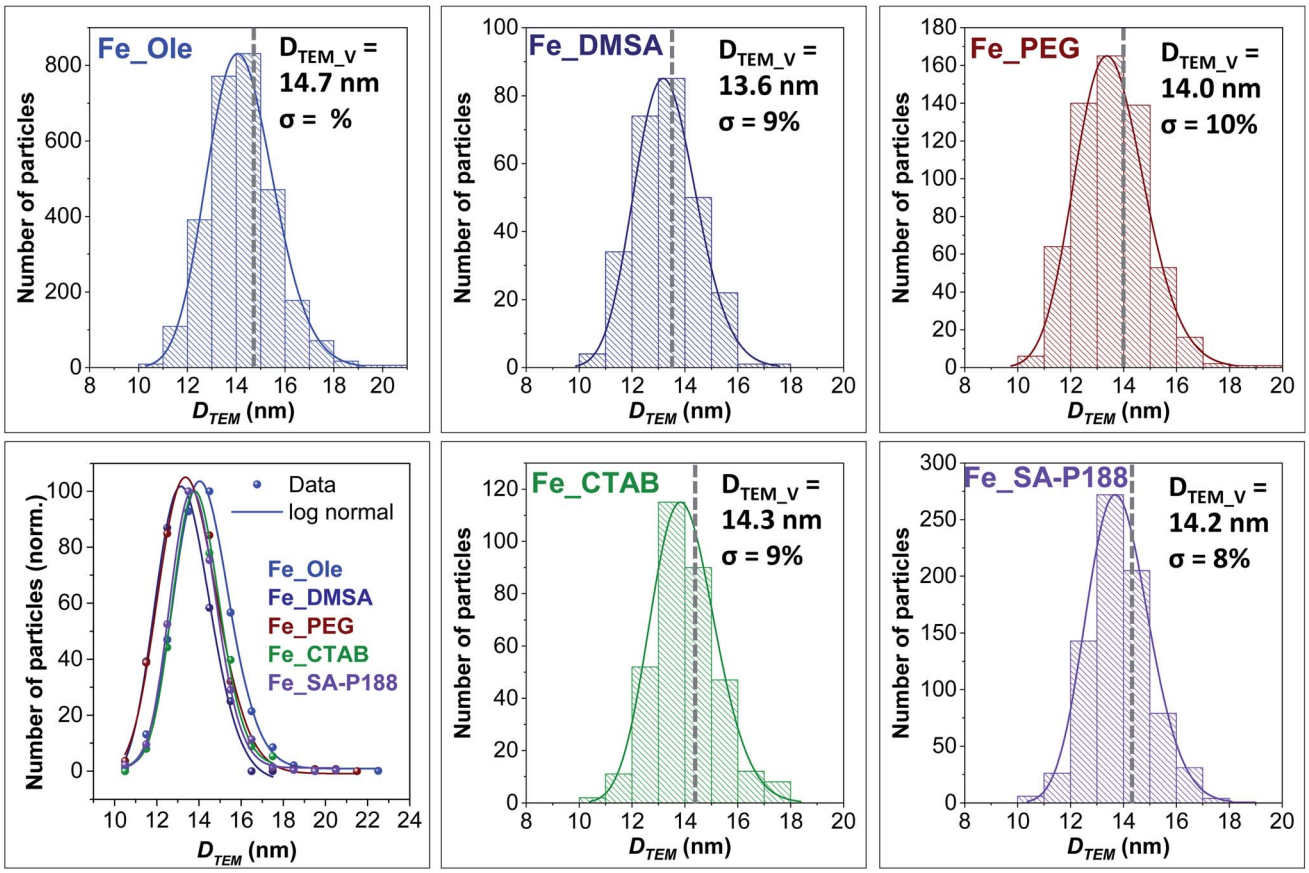

Fig. 2 Particle size distribution from TEM analysis with the dotted line representing the volume-weighted diameter of the sample before (Fe_Ole) and after functionalization (Fe_DMSA, Fe_PEG, Fe_CTAB, and Fe_SA-P188).

The Fe_Ole sample was modified with different organic molecules to make it hydrophilic: (i) ligand-exchange with PEGTMS (Fe_PEG) or (ii) ligand exchange with DMSA (Fe_DMSA); (iii) intercalation with CTAB (Fe_CTAB); (iv) intercalation with SA, and encapsulation in P188 (Fe_P188). The surface modification effectiveness was evaluated through FT-IR, TGA, DLS, ELS, and TEM analyses.

First of all, no changes in the size of the inorganic core and size distributions were detected upon functionalization (Fig. 2). Indeed, the slight variations in the particle sizes can be associated with possible differences in the image contrast derived from the different capping molecules.

The FTIR spectrum of Fe_Ole (Fig. 3) shows the main vibrational modes associated with the oleate molecules, as the COO^- vibrational modes (ν_{as} (COO^-) and ν_s (COO^-) at about 1529 and 1415 cm^{-1}, respectively) and those related to the hydrocarbon chain (2955 cm^{-1} for ν_{as} C–H(CH_3), 2922 cm^{-1} for ν_{as} C–H(CH_2), and 2852 cm^{-1} for ν_s C–H(CH_2)).[13,75] The bands centered at about 632 and 590 cm^{-1}, accompanied by three shoulders at 735, 695, and 560 cm^{-1}, are associated with the Fe–O stretching and indicate the presence of maghemite, in agreement with ^{57}Fe Mössbauer spectroscopy and XRD data.[30,33] The FT-IR spectrum of the DMSA-coated sample (Fig. 3a) revealed a series of absorption bands typical of carboxylic acids (1640–1370 cm^{-1} region), a shift (from 1700 cm^{-1} to 1740 cm^{-1}) of the carbonyl stretching, and a metal–oxygen stretching mode at around 590 cm^{-1}. The S–H stretching that should appear at about 2560 cm^{-1} is not visible due to the low amount and the weak intensity, S–H being a weak dipole.[76] The sharp reduction of alkyl bands in the DMSA-coated sample indicates the almost complete removal of oleate molecules.[77] The FT-IR spectrum of the PEG-coated sample is reported in Fig. 3b, showing the characteristic bands of PEGTMS in the region 1000–1100 cm^{-1}, especially the Si–O–Si and Si–OH stretching modes at 1100 and 946 cm^{-1}, respectively,[78] as well as the Fe–O stretching mode at 590 cm^{-1}. The FT-IR spectrum of the sample after the intercalation process with CTAB (Fig. 3c) shows the bands at 2944, 2918, and 2848 cm^{-1} associated with the different modes of the hydrocarbon chain (present in both oleate and CTAB), and the bands typical of CTAB in the region 1500–500 cm^{-1} besides the peak at 3016 cm^{-1} related to the N–CH_3 mode.[79] The band related to the Fe–O mode at 590 cm^{-1} is also visible; however it is very weak due to the high percentage of CTAB (95% w/w). The spectrum of the sample intercalated with stearic acid and encapsulated in poloxamer 188 is displayed in Fig. 3d, showing, besides the Fe–O mode at 590 cm^{-1}, the typical bands of the molecules. In particular, the C–H stretching modes at about 3000 cm^{-1} and the bands in the fingerprint region confirm the presence of P188, while the bands associated with stearic acid

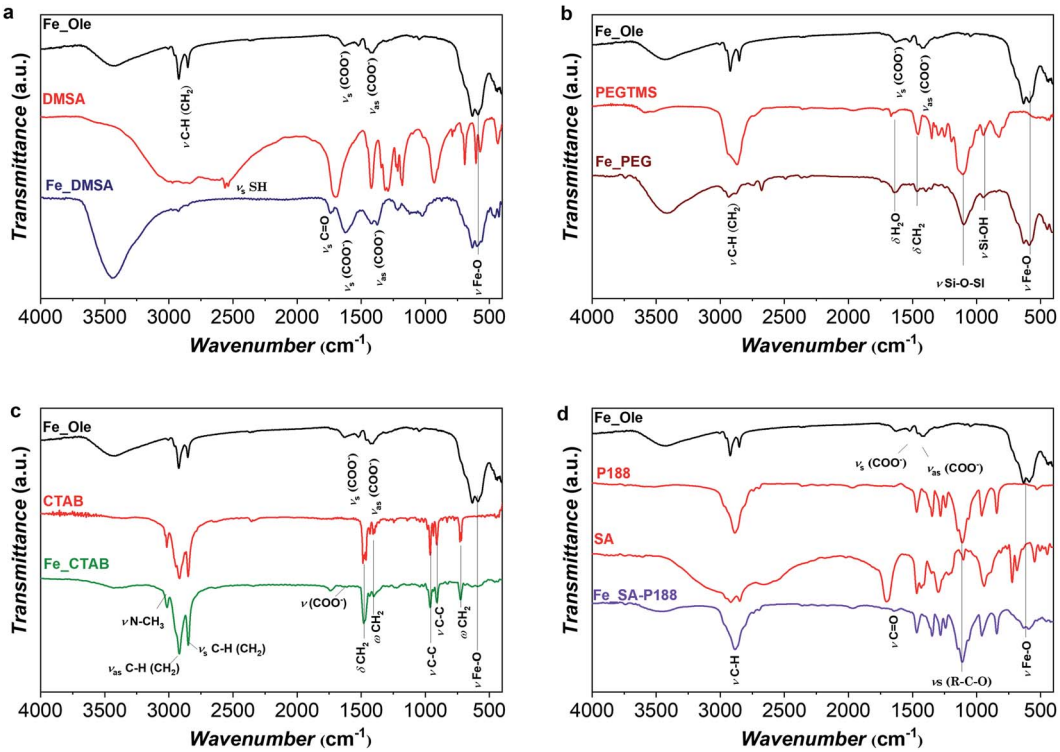

Fig. 3 FT-IR spectra of the oleate-capped Fe_Ole sample with the corresponding ligand after surface modification: DMSA (a), PEG (b), CTAB (c), and SA-P188 (d).

are more difficult to visualize, due to the lower amount (6%) with respect to P188.

Thermogravimetric analyses of the oleate coated samples, the molecules used for surface modification, and the samples after post-synthesis treatment are reported in Fig. 1S and 2S† to determine the organic content (Table 1) and the decomposition temperatures. The free molecule decompositions are all in the range 220–275 °C, with DMSA and CTAB having a smaller second step at about 450–470 °C. The oleate decomposition temperature for Fe_Ole is at about 240–250 °C, in agreement with results obtained for similar particles.[7,13,30,33] DMSA-coated particles undergo weight losses at 220 °C and 370 °C: the first one is close to the one of the free molecule, while the second one is shifted toward lower temperatures, indicating the bonding of DMSA to the maghemite, as also observed by other authors.[80,81] The PEG-coated sample reveals a decomposition temperature of about 240 °C, slightly higher compared to that of the free PEGTMS molecule, indicating bonding between PEG and the iron oxide surface. The CTAB-modified sample displays a two-step decomposition (at 250 and 450 °C), similar to those of the free-CTAB molecule, indicating the absence of strong bonds between NPs and molecules, typical of the intercalation process. Similar behavior is observed for the samples encapsulated in P188, with a weight loss in the range 130–300 °C as the free P188, even though the first derivative is shifted to lower temperature due to the presence of the oleate and stearic acid molecules.

DLS analyses on the colloidal dispersions of the surface-modified samples are shown in Fig. 4a and b, while the hydrodynamic diameter and the Brown relaxation times are

Table 1 TEM, DLS, ELS, magnetic measurements, and TGA of the surface-modified samples: volume-weighted particle size (D_{TEM_V}), hydrodynamic diameter calculated by number (D_{DLS_N}) and by volume (D_{DLS_V}), diffusion coefficient (D_C), Brown relaxation time (τ_B), zeta potential (ζ), anisotropy constant (K), Néel relaxation time (τ_N), effective relaxation time (τ_{eff}), blocking temperature (T_b), and organic content (OC) calculated from TGA

Sample	D_{TEM_V} (nm)	D_{DLS_N} (nm)	D_{DLS_V} (nm)	D_C (μ^2/s)	τ_B (s)	ζ (mV)	$K \times 10^3$ (J m^{-3})	τ_N (s)	τ_{eff} (s)	T_b (K)	OC (% w/w)
Fe_DMSA	13.6(1.2)	14(3)	17(5)	12.8(3)	$8(2) \times 10^{-7}$	−29(1)	3.1(3)	$6.7(6) \times 10^{-5}$	$8(2) \times 10^{-7}$	105(2)	7(1)
Fe_PEG	14.0(1.3)	17(5)	22(9)	19.3(1)	$1.5(4) \times 10^{-6}$	−30(1)	2.3(2)	$1.5(1) \times 10^{-5}$	$1.4(4) \times 10^{-6}$	89(2)	18(2)
Fe_CTAB	14.3(1.2)	25(7)	38(30)	5.9(1)	$5(1) \times 10^{-6}$	+44(2)	2.2(3)	$1.5(1) \times 10^{-5}$	$3.7(8) \times 10^{-6}$	87(2)	95(5)
Fe_SA-P188	14.2(1.2)	59(16)	75(26)	6.1(1)	$6(2) \times 10^{-5}$	−10(1)	2.2(3)	$1.5(1) \times 10^{-5}$	$1.2(4) \times 10^{-5}$	87(2)	82(4)

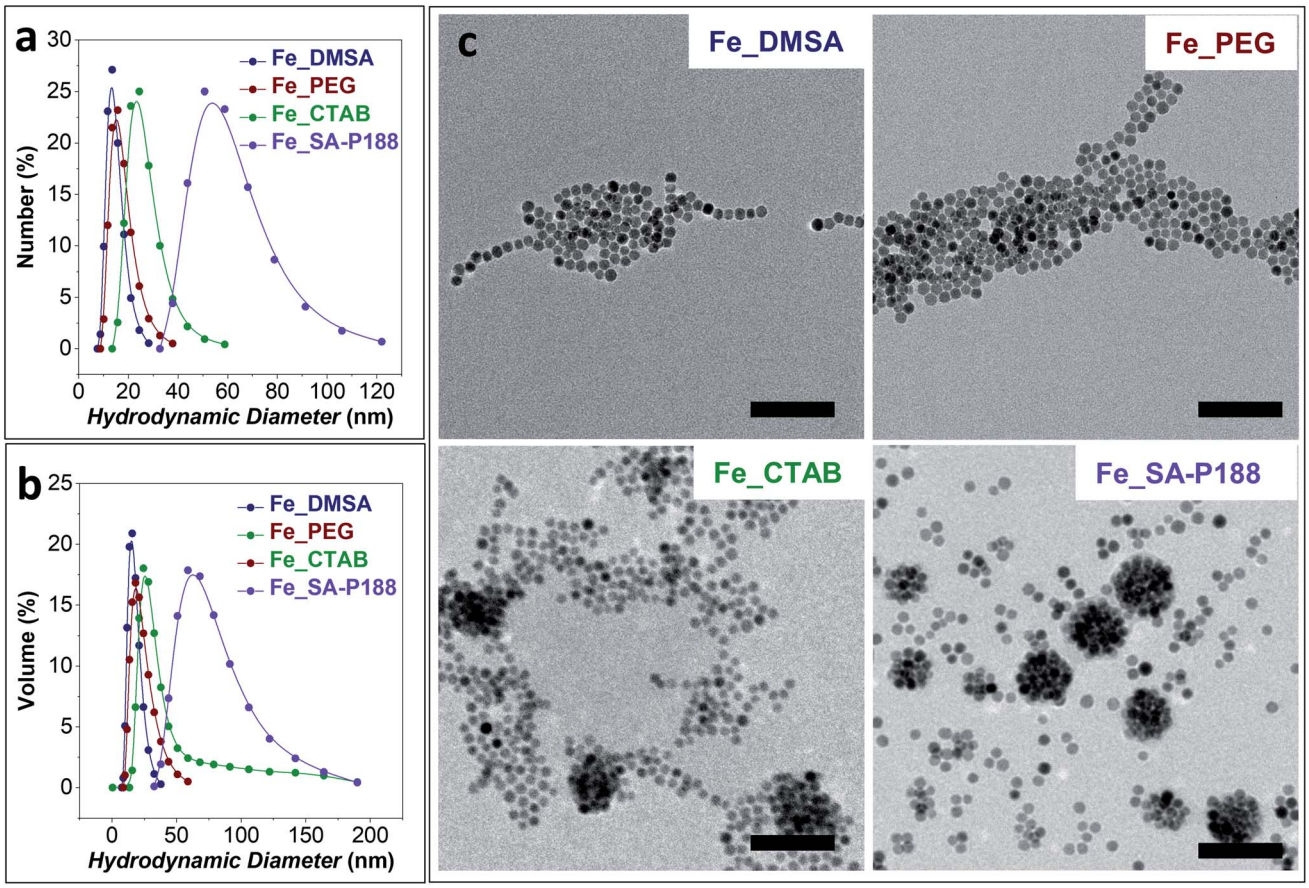

Fig. 4 (a) Number distribution and (b) volume distribution of the hydrodynamic diameter of the samples obtained by the DLS measurements. (c) TEM images of the samples after surface modification. The scale bars correspond to 100 nm.

shown in Table 1. The Fe_SA-P188 sample presents the largest clusters, having a hydrodynamic diameter of about 60 nm and the slowest Brown relaxation ($\tau_B = 6.0 \times 10^{-5}$ s). This scenario corroborates the hypothesis of the intercalation of stearic acid between the oleate molecules capping the iron oxide NP surface and the encapsulation of several of them by poloxamer 188. The other samples present a smaller hydrodynamic diameter, suggesting the presence of isolated NPs. In particular, the smallest hydrodynamic diameter (and the lowest τ_B) was obtained for the DMSA and PEG-coated samples produced by the ligand exchange process instead of intercalation. It is worth noting that all samples present constant values with time, a monomodal distribution, and no sedimentation, indicating the stability of the aqueous colloidal dispersions.

The TEM images of the modified samples are reported in Fig. 4c. Both DMSA- and PEG-coated samples featured isolated particles with the absence of clusters. In contrast, in the CTAB-coated sample's micrograph, some clusters of about 80 nm are visible. Nevertheless, a large number of separated particles are present. For this reason, the mean diameter estimated from DLS measurements in terms of the number of particles is in the range of 20–30 nm. The existence of the 80 nm clusters also in the aqueous dispersion is confirmed by the volume distribution of hydrodynamic diameters (Fig. 4b and Table 1) that features a long tail at higher D_{DLS} values. Well-defined spherical clusters of NPs of about 60–70 nm are observable in the P188 modified sample due to the encapsulation of the particles inside the polymer. The low content of separated particles also enables the match between the observed TEM size and the hydrodynamic diameter calculated by DLS both by number and volume distributions.

ELS analyses were performed on the modified samples to estimate the zeta potential (ζ, Table 1). The CTAB-modified sample features positive values due to the presence of quaternary ammonium,[82–88] thus confirming effective intercalation. In contrast, DMSA-coated NPs reveal negative values because of the thiol group of DMSA molecules.[14,77,89] Fe_PEG also shows negative values. Even though no acidic or basic functions are present in the molecule, other authors observed the same behavior, ascribing it to incorporating hydroxide ions into the PEG layer[90] or to ionizable hydroxyl groups on the iron oxide surface.[64] Also, the P188-modified sample reveals a negative zeta potential value, probably for the same reasons, but no data are available in the literature for comparison.

The temperature dependence of the magnetization was studied through ZFC–FC protocols directly on the dispersions with a concentration identical to that used for the heating experiments (Fig. 3S†). Despite the minor differences among the aqueous dispersions, all samples possess a similar temperature dependence of the magnetization. The curves show

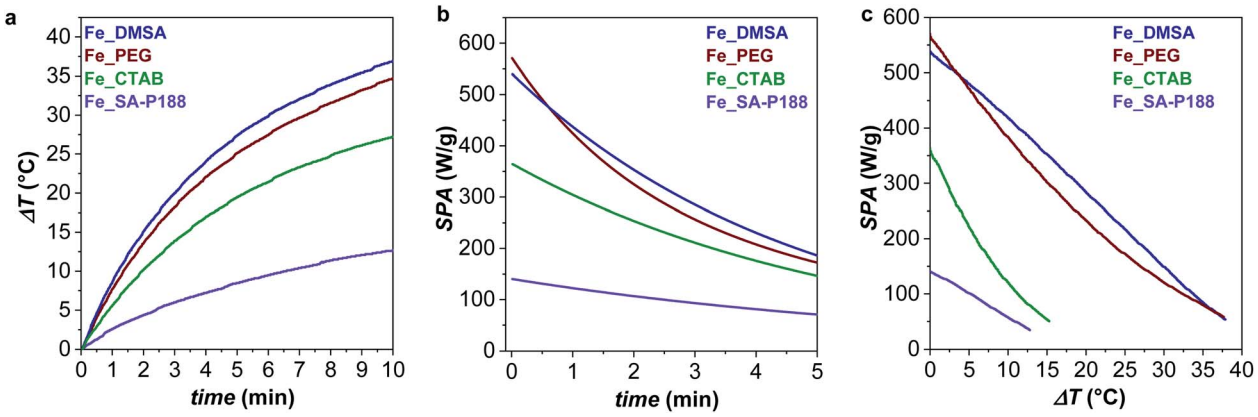

Fig. 5 (a) Heat dissipation of the aqueous colloidal dispersion (1.12 mg mL^{-1}) measured at 316 G and 782 kHz; (b) SPA evolution of the samples with time and temperature (c) for the curves recorded at 782 kHz and 316 G. The heat dissipation curves at various frequencies and amplitude of the applied magnetic field are reported in Fig. 5S and 6S.†

a jump in the temperature range 260–280 K due to the melting of water and a maximum temperature of about 190 ± 10 K for all samples (Fig. 4Sa†). The distribution of blocking temperatures (Fig. 4Sb†) reveals a T_b centered at 88 ± 2 K for Fe_PEG, Fe_CTAB, and Fe_SA-P188 samples, while a slightly shifted distribution (T_b = 105 ± 2 K) is observed for Fe_DMSA, probably because of the shorter chain of the DMSA molecule that can cause stronger interparticle interactions. The anisotropy constants (K) calculated from T_b through eqn (6) are in the range 2 to 3 × 10^3 J m^{-3}, close to the bulk maghemite (5 × 10^3 J m^{-3}). The Néel relaxation times (τ_N), calculated utilizing eqn (1), are all in the order of 10^{-5} s, indicating high magnetic similarities among the samples. As a consequence, the effective relaxation time (τ_{eff}, eqn (3)) depends mainly on the τ_B, and it was found to be faster for Fe_DMSA (8 × 10^{-7} s), followed by Fe_PEG (1.5 × 10^{-6} s), Fe_CTAB (1.4 × 10^{-6} s), and Fe_SA-P188 (1.2 × 10^{-5} s). All FC curves feature a temperature-independent behavior up to 200 K (curve flatness), indicating strong interparticle interactions, as already observed for CTAB-intercalated core–shell spinel ferrite NPs.[7] Note that the concentration of the NPs in the dispersions is rather high, and the interparticle interactions become important.

At room temperature, the samples do not exhibit hysteretic behaviour (measurements not shown), indicating a SPM regime in the DC magnetometry time window. It is important to note that superparamagnetism is a time- and frequency-dependent phenomenon. While the samples exhibit SPM behavior in the time window of DC magnetometry (0.001–1 s), if other techniques with a faster time window are used, the samples might appear in the blocked state. For instance, in the room temperature ^{57}Fe Mössbauer spectrum of Fe_Ole a sextet is present (Fig. 1d), due to particles in the blocked state, in the measurement time window of 10^{-9} to 10^{-7} s.

Magnetic field-induced heating

The set of samples represents an ideal case study, all made up of the same non-toxic magnetic core with low size dispersity and water stability but featuring different capping molecules, aggregation states, hydrodynamic sizes, and Brown relaxation times. Therefore, all aqueous sample dispersions (1.12 mg mL^{-1}) were tested as heat mediators under an applied alternating magnetic field of 100, 200, 316, or 400 G, and at frequencies of 159, 330, 497, 639, or 782 kHz. The heating curves at 316 G and 782 kHz are reported in Fig. 5, while ΔT, SPA, and ILP values are shown in Table 2.

At 782 kHz and 316 G, the highest SPA values are observed for the samples coated with DMSA and PEG molecules that reach 539 and 571 W g^{-1}, respectively. Considering the limitations of the parameter intrinsic loss power (ILP), which can be applied only on superparamagnetic systems and in the frame of the linear response theory, it represents a helpful tool for comparing data acquired at different frequencies and amplitudes.[13,39,91] The calculated ILP values are reported in Table 2, while a comparison with data reported in the literature for similar systems is shown in Table 1S.† Even though DMSA is a commonly employed coating molecule for stabilizing NPs in water, ILP values above 1.1 nH m^2 kg_{ox}^{-1} have never been observed in the literature (Table 1S†).[35–39] In contrast, Fe_SA-P188 features the lowest ΔT and SPA value (140 W g^{-1}), which is most likely correlated with the formation of spherical clusters as recognized by TEM and DLS analyses (Fig. 4). It is known that the formation of secondary entities (clusters) affects the heating abilities[7,38] due to the slower Brown relaxation time (Table 1). The CTAB-intercalated sample reveals a heating efficiency in the middle, in line with the presence of some clusters and faster τ_B than that of Fe_SA-P188 and slower than that of Fe_PEG and Fe_DMSA.

The initial SPA values for all samples follow the theoretical frequency dependence (eqn (4)) in the range 159–782 kHz (Fig. 6a), obtaining the best fit for Fe_DMSA (R^2 = 0.998) and the worst for Fe_SA-P188 (R^2 = 0.90). For some samples, *e.g.*, Fe_DMSA and Fe_CTAB, the dependence is almost linear in the studied frequency range. Even though only minor differences can be observed in the heating abilities as a function of frequency for Fe_DMSA and Fe_PEG, it seems that Fe_DMSA is the most efficient sample at low frequencies (50% and 20% more

Table 2 Experimental conditions of the heat release test of water colloidal dispersions (1.12 mg mL^{-1}) of modified samples. Temperature increases after 10 minutes of applying an alternating magnetic field (ΔT), specific power absorption (SPA), and intrinsic loss power (ILP). The final temperatures reached are reported in Table 2S

Experimental conditions	159 kHz, 316 G			330 kHz, 316 G			497 kHz, 316 G			639 kHz, 316 G			782 kHz, 316 G		
Sample	ΔT (°C)	SPA (W g^{-1})	ILP ([a])	ΔT (°C)	SPA (W g^{-1})	ILP ([a])	ΔT (°C)	SPA (W g^{-1})	ILP ([a])	ΔT (°C)	SPA (W g^{-1})	ILP ([a])	ΔT (°C)	SPA (W g^{-1})	ILP ([a])
Fe_DMSA	4.2	62	0.61	11.5	191	0.91	19.9	324	1.02	—	—	—	36.9	539	1.08
Fe_PEG	2.7	31	0.31	9.4	154	0.73	17.3	311	0.98	25.1	379	0.93	34.7	571	1.14
Fe_CTAB	3.1	32	0.32	8.5	116	0.55	15.1	182	0.58	21.7	271	0.66	27.2	364	0.73
Fe_SA-P188	—	—	—	2.8	27	0.13	5.6	62	0.20	10.6	151	0.37	12.7	140	0.28

[a] nH m^2 kg_{ox}^{-1}.

efficient at 159 and 330 kHz, respectively). In comparison, at higher frequencies, they become comparable (4–6% differences at 497–782 kHz). One possible explanation could be related to the slower Néel relaxation time of Fe_DMSA compared to Fe_PEG (1.4×10^{-6} *vs.* 8×10^{-7} s), which may be responsible for slightly better efficiency at low frequency. Nevertheless, it must be highlighted that both samples behave in a very similar way, in agreement with the small differences in magnetic and colloidal properties (which are reflected in τ_B and τ_N).

For the Fe_PEG sample, the dependency of the SPA on the amplitude of the magnetic field follows the square low SPA = αH^x, where x was found to be 1.9, very close to the theoretical value of 2, as also observed by other authors (Fig. 6b).[39,92]

By looking at the ILP frequency dependence (Fig. 6c), one would expect no variation of ILP; instead, we observed its gradual increase with the frequency (the data were fitted with eqn (4)), clearly indicating a deviation from linear response theory. Also, other authors observed a nonlinear behavior of the susceptibility imaginary part with the frequency that can cause the nonconstant response of the ILP.[93–95] For all samples except Fe_SA-P188, the maximum ILP is reached at the maximum frequency. For Fe_SA-P188, in contrast, 639 kHz is the most efficient frequency. Concerning the evolution of ILP with the applied field amplitude (Fig. 6d), the tendency is not constant. Still, it follows an exponential decay, reaching the maximum for Fe_PEG (ILP = 1.74 nH m^2 kg_{ox}^{-1}) at 100 G and becoming almost constant at 316 and 400 G (ILP = 0.95 ± 0.02 nH m^2 kg_{ox}^{-1}). In contrast, de la Presa *et al.* observed an initial increase of ILP with H_0, and then a steady behavior in the range 40–90 G, and therefore below the range of the magnetic fields applied in this work. In this latter case, they analyzed 13 nm-uncoated maghemite nanoparticles having an aggregate size, estimated by DLS, in the range 60–75 nm.[95]

Magnetic field-induced heating is a complex process. In addition, for these samples, we can hypothesize both relaxations (linear response theory) and hysteresis losses as responsible for the heat release but with no information on their relative importance, considering the frequency of the alternating magnetic field. Indeed, the frequency range employed in this study for the heat dissipation (159–782 kHz) corresponds to a time window of 1×10^{-6} to 2×10^{-7} s, just above the Mössbauer measurement time window, and it is reasonable to expect that at least a part of the NPs' population was not in the SPM state. In addition, aggregation phenomena, often occurring in colloidal magnetic dispersion, can make the understanding of mechanisms even more complex. In our case, a comparison among the samples and the effect of the molecular coating can be carried out with high reliability as all samples are based on the same inorganic core and, therefore, the same size, also kept after the surface functionalization. Therefore, all the effects derived from the different organic coatings on the magnetic and colloidal properties are summed up in the obtained heat response, although it is not possible to discern the contribution of single parameters. Additional information on the heat response efficiency can also be extracted by following the evolution of the SPA with time and temperature since the colloidal dispersions of magnetic NPs are dynamic systems. Beyond the initial SPA values, the SPA dependences on time and temperature are shown, for the curves recorded at 782 kHz and 316 G, in Fig. 5; the curves recorded at the other frequencies and amplitudes are reported in Fig. 6S–8S.†

By looking at Fig. 5b, it is possible to observe that the heat release gradually decreases with increasing time and temperature. Still, clear differences can be identified between the samples. For instance, Fe_PEG shows a more pronounced initial decrease, so it features the highest SPA value in the initial phase. However, after just 30 seconds, there is an inversion with Fe_DMSA, which becomes the sample with the overall highest heat release. Similar sharp decreases can be observed for other frequencies and samples, for instance, at 639 kHz for Fe_SA-P188, at 497 kHz for Fe_PEG, 330 kHz for Fe_CTAB 330, and 497 kHz for Fe_DMSA.

Interestingly, these are also the points that deviate the most from the initial ILP *vs.* frequency plots (Fig. 6c, red arrows), corroborating the hypothesis that the initial heating stage does not truly represent the whole heat dissipation phenomenon. The anomalous trends are clearly visible in Fig. 8S,† where the SPA *vs.* temperature graphs for different frequencies of the applied alternating magnetic field are shown. Although they generally follow a straight line, a kink emerges for some frequencies specific to each sample (highlighted by black arrows). It seems that under those experimental conditions, a higher response at the beginning of the heat dissipation is observed, as in part predicted by fitting with eqn (4), where the

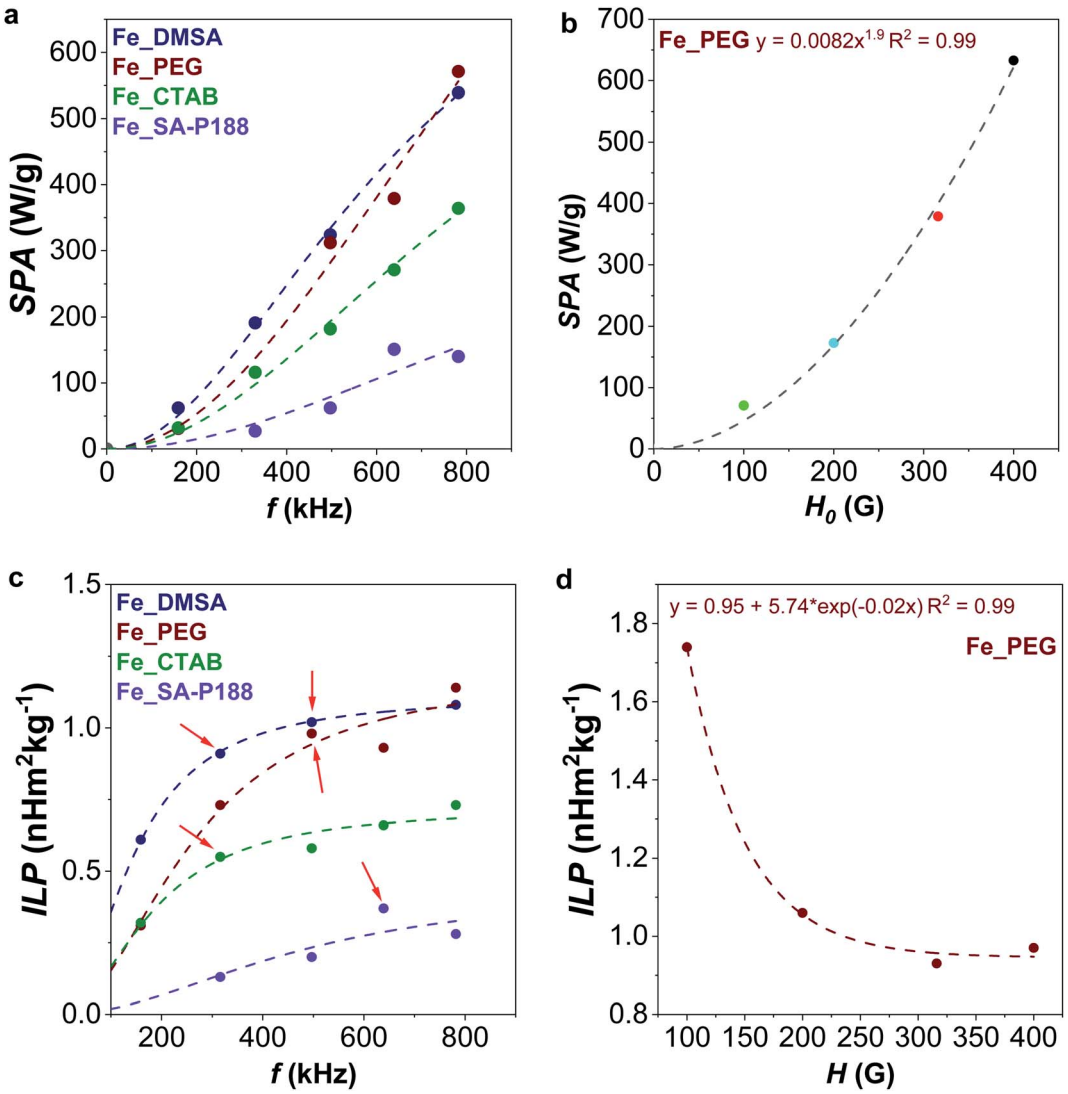

Fig. 6 Evolution of SPA with frequency (a, at 316 G, fitted with eqn (4)) and amplitude (b, at 639 kHz, fitted with a power law) of the applied alternating magnetic field. Evolution of ILP with frequency (c, at 316 G, fitted with eqn (4)) and amplitude (d, at 639 kHz, fitted with exponential decay) of the applied alternating magnetic field.

curve bends, which then gradually decreases and follows the general linear trend of the other frequencies. The observed anomalies could also be caused by the possible occurrence of hysteretic losses, as already explained.

For this reason, the evolution of ILP with time, reported in Fig. 9S,† reveals some crucial aspects. In the beginning, there is a separation of ILP *vs.* time curves for the different frequencies, but the curves converge when approaching a kind of steady state. For instance, after 9 minutes, the ILP of both Fe_DMSA and Fe_PEG is equal to 0.17 ± 0.02 nH m^2 kg^{-1}, for Fe_CTAB is 0.13 ± 0.02 nH m^2 kg^{-1}, and for Fe_SA-P188 is 0.07 ± 0.02 nH m^2 kg^{-1}, considering all the frequencies. The standard deviation of the mean value for each sample (± 0.02 nH m^2 kg^{-1}) would be even better if the slowest frequency is neglected since it introduces the highest uncertainty.

Therefore, the evolution of SPA *vs.* time and temperature permits understanding how the NPs behave at different frequencies. In contrast, the ILP *vs.* time curves enable an easier and more reliable comparison among the samples when each NP system acts independently of the frequency (*e.g.*, after 9 min).

Conclusions

In this work, 15 nm oleate-capped maghemite NPs were prepared by a seed-mediated growth method under solvothermal conditions, and then made hydrophilic through modification with polyethylene glycol (PEG), dimercaptosuccinic acid (DMSA), cetrimonium bromide (CTAB), or stearic acid (SA) and poloxamer 188 (P188). Ligand exchange procedures with PEG and DMSA permitted the NPs to be kept isolated, while intercalation with CTAB and SA and encapsulation with P188 led to agglomeration into spherical clusters. The aqueous dispersions were tested for heating abilities under adiabatic conditions in an alternating magnetic field with different frequencies and amplitudes. The results showed

higher initial performances for the samples with no clustering phenomena (PEG and DMSA) and lower performances for CTAB and SA-P188, in line also with the Brown relaxation times of the particles, highlighting the detrimental effect of a cluster of NPs where there is no magnetic order. Moreover, an appropriate selection of the frequency, amplitude, and time of the AMF permitted the tuning of the final temperature from room temperature to 60 °C. Furthermore, the evolution of SPA and ILP with frequency and amplitude was followed as a function of the time and the temperature. The character of the heating curves was found to help understand how the NPs behave since the kinks correspond to the inflection points of the frequency dependency of the power loss. Moreover, a convergence of the ILP *vs.* time curves suggests that the system behaves independently of the frequency after a certain time, allowing a direct comparison among all samples within the series. These results highlighted how a deeper understanding of the heat dissipation phenomenon is possible by analyzing in detail both the initial SPA and ILP values and their evolution with time and temperature, besides the frequency and the amplitude of the applied alternating magnetic field.

Conflicts of interest

There are no conflicts to declare.

Acknowledgements

The CESA Project – RAS Piano Sulcis (CUP E58C16000080003) is gratefully acknowledged for financing the post-doctoral fellowships of M. Sanna Angotzi. PON AIM (PON Ricerca e Innovazione 2014–2020-Azione I.2-D.D. n.407 del 27 Febbraio 2018 "Attraction and International Mobility", Cult-GeoChim project no. AIM1890410-3) is gratefully acknowledged for financing the fixed-term researcher fellowship of V. Mameli. Thanks are due to Dr Andrea Ardu and Centro Servizi di Ateneo per la Ricerca (CeSAR) for using the electron microscopes Jeol JEM 1400 Plus and Jeol JEM 2010 UHR. The Fondazione di Sardegna (FdS) is acknowledged for the financial support – Project: CUP F72F20000240007(2019): "Surface-tailored Materials for Sustainable Environmental Applications". The authors also acknowledge the support provided by the Research Infrastructures MGML (Project no. LM2018096) and European Research Council (ERC-Stg-716265).

Notes and references

1 C. Cara, E. Rombi, A. Musinu, V. Mameli, A. Ardu, M. Sanna Angotzi, L. Atzori, D. Niznansky, H. L. Xin and C. Cannas, *J. Mater. Chem. A*, 2017, **5**, 21688–21698.
2 M. Vacca, C. Cara, V. Mameli, M. Sanna Angotzi, M. Scorciapino, M. G. Cutrufello, A. Musinu, V. Tyrpekl, L. Pala and C. Cannas, *ACS Sustainable Chem. Eng.*, 2020, **8**, 14286–14300.
3 C. Cara, E. Rombi, V. Mameli, A. Ardu, M. Sanna Angotzi, D. Niznansky, A. Musinu and C. Cannas, *J. Phys. Chem. C*, 2018, **122**, 12231–12242.
4 C. Cara, V. Mameli, E. Rombi, N. Pinna, M. Sanna Angotzi, D. Nižňanský, A. Musinu and C. Cannas, *Microporous Mesoporous Mater.*, 2020, **298**, 110062.
5 M. Sanna Angotzi, V. Mameli, C. Cara, K. B. L. Borchert, C. Steinbach, R. Boldt, D. Schwarz and C. Cannas, *Nanoscale Adv.*, 2021, **3**, 6100–6113.
6 N. Lee, D. Yoo, D. Ling, M. H. Cho, T. Hyeon and J. Cheon, *Chem. Rev.*, 2015, **115**, 10637–10689.
7 M. Sanna Angotzi, V. Mameli, C. Cara, A. Musinu, C. Sangregorio, D. Niznansky, H. L. Xin, J. Vejpravova and C. Cannas, *Nanoscale Adv.*, 2020, **2**, 3191–3201.
8 M. Sanna Angotzi, V. Mameli, C. Cara, D. Peddis, H. L. Xin, C. Sangregorio, M. L. Mercuri and C. Cannas, *Nanoscale Adv.*, 2021, **3**, 1612–1623.
9 A. Kirschning, L. Kupracz and J. Hartwig, *Chem. Lett.*, 2012, **41**, 562–570.
10 R. B. N. Baig and R. S. Varma, *Chem. Commun.*, 2013, **49**, 752–770.
11 V. Polshettiwar, R. Luque, A. Fihri, H. Zhu, M. Bouhrara and J. M. Basset, *Chem. Rev.*, 2011, **111**, 3036–3075.
12 D. Zhang, C. Zhou, Z. Sun, L.-Z. Wu, C.-H. Tung and T. Zhang, *Nanoscale*, 2012, **4**, 6244.
13 V. Mameli, A. Musinu, A. Ardu, G. Ennas, D. Peddis, D. Niznansky, C. Sangregorio, C. Innocenti, N. T. K. Thanh and C. Cannas, *Nanoscale*, 2016, **8**, 10124–10137.
14 M. Avolio, A. Guerrini, F. Brero, C. Innocenti, C. Sangregorio, M. Cobianchi, M. Mariani, F. Orsini, P. Arosio and A. Lascialfari, *J. Magn. Magn. Mater.*, 2019, **471**, 504–512.
15 E. Fantechi, C. Innocenti, M. Zanardelli, M. Fittipaldi, E. Falvo, M. Carbo, V. Shullani, L. Di Cesare Mannelli, C. Ghelardini, A. M. Ferretti, A. Ponti, C. Sangregorio and P. Ceci, *ACS Nano*, 2014, **8**, 4705–4719.
16 R. E. Rosensweig, *J. Magn. Magn. Mater.*, 2002, **252**, 370–374.
17 R. Hergt, S. Dutz and M. Zeisberger, *Nanotechnology*, 2010, **21**, 015706.
18 J. Carrey, B. Mehdaoui and M. Respaud, *J. Appl. Phys.*, 2011, **109**, 083921.
19 C. L. Dennis, A. J. Jackson, J. A. Borchers, R. Ivkov, A. R. Foreman, J. W. Lau, E. Goernitz and C. Gruettner, *J. Appl. Phys.*, 2008, **103**, 2–5.
20 A. Y. Zubarev, *Phys. Rev. E*, 2018, **98**, 032610.
21 B. Mehdaoui, R. P. Tan, A. Meffre, J. Carrey, S. Lachaize, B. Chaudret and M. Respaud, *Phys. Rev. B: Condens. Matter Mater. Phys.*, 2013, **87**, 1–10.
22 D. Serantes, K. Simeonidis, M. Angelakeris, O. Chubykalo-Fesenko, M. Marciello, M. Del Puerto Morales, D. Baldomir and C. Martinez-Boubeta, *J. Phys. Chem. C*, 2014, **118**, 5927–5934.
23 A. F. Abu-Bakr and A. Y. Zubarev, *J. Magn. Magn. Mater.*, 2019, **477**, 404–407.
24 C. Blanco-Andujar, D. Ortega, P. Southern, Q. A. Pankhurst and N. T. K. K. Thanh, *Nanoscale*, 2015, **7**, 1768–1775.
25 L. C. Branquinho, M. S. Carrião, A. S. Costa, N. Zufelato, M. H. Sousa, R. Miotto, R. Ivkov and A. F. Bakuzis, *Sci. Rep.*, 2013, **3**, 20–22.
26 C. Haase and U. Nowak, *Phys. Rev. B: Condens. Matter Mater. Phys.*, 2012, **85**, 2–6.

27 B. Mehdaoui, A. Meffre, J. Carrey, S. Lachaize, L.-M. Lacroix, M. Gougeon, B. Chaudret and M. Respaud, *Adv. Funct. Mater.*, 2011, **21**, 4573–4581.
28 V. Mameli, M. Sanna Angotzi, C. Cara and C. Cannas, *J. Nanosci. Nanotechnol.*, 2019, **19**, 4857–4887.
29 M. Fantauzzi, F. Secci, M. Sanna Angotzi, C. Passiu, C. Cannas and A. Rossi, *RSC Adv.*, 2019, **9**, 19171–19179.
30 M. Sanna Angotzi, V. Mameli, C. Cara, A. Ardu, D. Nizňnanský and A. Musinu, *J. Nanosci. Nanotechnol.*, 2019, **19**, 4954–4963.
31 M. Sanna Angotzi, V. Mameli, A. Musinu and D. Nizňnanský, *J. Nanosci. Nanotechnol.*, 2019, **19**, 5008–5013.
32 M. Sanna Angotzi, V. Mameli, D. Zákutná, D. Kubániová, C. Cara and C. Cannas, *J. Phys. Chem. C*, 2021, **125**, 20626–20638.
33 M. Sanna Angotzi, A. Musinu, V. Mameli, A. Ardu, C. Cara, D. Niznansky, H. L. Xin and C. Cannas, *ACS Nano*, 2017, **11**, 7889–7900.
34 M. Sanna Angotzi, V. Mameli, C. Cara, V. Grillo, S. Enzo, A. Musinu and C. Cannas, *Sci. Rep.*, 2020, **10**, 17015.
35 V. Nandwana, S. R. Ryoo, S. Kanthala, M. De, S. S. Chou, P. V. Prasad and V. P. Dravid, *ACS Appl. Mater. Interfaces*, 2016, **8**, 6953–6961.
36 Z. Surowiec, A. Miaskowski and M. Budzyński, *Nukleonika*, 2017, **62**, 183–186.
37 D. F. Coral, P. Mendoza Zélis, M. Marciello, M. D. P. Morales, A. Craievich, F. H. Sánchez and M. B. Fernández Van Raap, *Langmuir*, 2016, **32**, 1201–1213.
38 L. L. Gutiérrez, L. de la Cueva, M. Moros, E. Mazarío, S. de Bernardo, J. M. de la Fuente, M. P. Morales and G. Salas, *Nanotechnology*, 2019, **30**, 112001.
39 M. Avolio, A. Guerrini, F. Brero, C. Innocenti, C. Sangregorio, M. Cobianchi, M. Mariani, F. Orsini, P. Arosio and A. Lascialfari, *J. Magn. Magn. Mater.*, 2019, **471**, 504–512.
40 T. K. Oanh Vuong, T. T. Le, H. D. Do, X. T. Nguyen, X. C. Nguyen, T. T. Vu, T. L. Le and D. L. Tran, *Mater. Chem. Phys.*, 2020, **245**, 122762.
41 F. Mérida, C. Rinaldi, E. J. Juan and M. Torres-Lugo, *Int. J. Nanomed.*, 2020, **15**, 419–432.
42 L. Storozhuk and N. Iukhymenko, *Appl. Nanosci.*, 2019, **9**, 889–898.
43 J. M. Orozco-Henao, D. Muraca, F. H. Sánchez and P. Mendoza Zélis, *J. Phys. D: Appl. Phys.*, 2020, **53**, 385001.
44 M. E. de Sousa, A. Carrea, P. Mendoza Zélis, D. Muraca, O. Mykhaylyk, Y. E. Sosa, R. G. Goya, F. H. Sánchez, R. A. Dewey and M. B. Fernández van Raap, *J. Phys. Chem. C*, 2016, **120**, 7339–7348.
45 E. Cheraghipour and M. Pakshir, *J. Environ. Chem. Eng.*, 2021, **9**, 104883.
46 L. M. Bauer, S. F. Situ, M. A. Griswold and A. C. S. Samia, *Nanoscale*, 2016, **8**, 12162–12169.
47 A. Skumiel, K. Kaczmarek, D. Flak, M. Rajnak, I. Antal and H. Brząkała, *J. Mol. Liq.*, 2020, **304**, 0–5.
48 P. H. Linh, N. X. Phuc, L. V. Hong, L. L. Uyen, N. V. Chien, P. H. Nam, N. T. Quy, H. T. M. Nhung, P. T. Phong and I. J. Lee, *J. Magn. Magn. Mater.*, 2018, **460**, 128–136.
49 Z. Shaterabadi, G. Nabiyouni and M. Soleymani, *Mater. Sci. Eng., C*, 2020, **117**, 111274.
50 E. Illés, M. Szekeres, I. Y. Tóth, Á. Szabó, B. Iván, R. Turcu, L. Vékás, I. Zupkó, G. Jaics and E. Tombácz, *J. Magn. Magn. Mater.*, 2018, **451**, 710–720.
51 R. D. Piazza, W. R. Viali, C. C. dos Santos, E. S. Nunes, R. F. C. Marques, P. C. Morais, S. W. da Silva, J. A. H. Coaquira and M. Jafelicci, *Mater. Res. Express*, 2020, **7**, 015078.
52 M. Kishimoto, R. Miyamoto, T. Oda, H. Yanagihara, N. Ohkohchi and E. Kita, *J. Magn. Magn. Mater.*, 2016, **398**, 200–204.
53 L. H. Nguyen, V. T. K. Oanh, P. H. Nam, D. H. Doan, N. X. Truong, N. X. Ca, P. T. Phong, L. V. Hong and T. D. Lam, *J. Nanopart. Res.*, 2020, **22**, 258.
54 V. Ganesan, B. B. Lahiri, C. Louis, J. Philip and S. P. Damodaran, *J. Mol. Liq.*, 2019, **281**, 315–323.
55 M. Cobianchi, A. Guerrini, M. Avolio, C. Innocenti, M. Corti, P. Arosio, F. Orsini, C. Sangregorio and A. Lascialfari, *J. Magn. Magn. Mater.*, 2017, **444**, 154–160.
56 D. Sakellari, K. Brintakis, A. Kostopoulou, E. Myrovali, K. Simeonidis, A. Lappas and M. Angelakeris, *Mater. Sci. Eng., C*, 2016, **58**, 187–193.
57 A. F. Alves, S. G. Mendo, L. P. Ferreira, M. H. Mendonça, P. Ferreira, M. Godinho, M. M. Cruz and M. D. Carvalho, *J. Nanopart. Res.*, 2016, **18**, 1–13.
58 I. Khmara, M. Molcan, A. Antosova, Z. Bednarikova, V. Zavisova, M. Kubovcikova, A. Jurikova, V. Girman, E. Baranovicova, M. Koneracka and Z. Gazova, *J. Magn. Magn. Mater.*, 2020, **513**, 167056.
59 M. Soleymani, M. Velashjerdi, Z. Shaterabadi and A. Barati, *Carbohydr. Polym.*, 2020, **237**, 116130.
60 R. R. Koli, N. G. Deshpande, D. S. Kim, A. R. Shelke, A. V. Fulari, V. J. Fulari and H. K. Cho, *Ceram. Int.*, 2020, **46**, 24290–24301.
61 C. Cannas, A. Ardu, A. Musinu, L. Suber, G. Ciasca, H. Amenitsch and G. Campi, *ACS Nano*, 2015, **9**, 7277–7286.
62 L. Gomez, C. De Weerd, J. L. Hueso and T. Gregorkiewicz, *Nanoscale*, 2017, **9**, 631–636.
63 F. Carlà, G. Campo, C. Sangregorio, A. Caneschi, C. de Julián Fernández and L. I. Cabrera, *J. Nanopart. Res.*, 2013, **15**, 1813.
64 E. K. U. Larsen, T. Nielsen, T. Wittenborn, H. Birkedal, T. Vorup-Jensen, M. H. Jakobsen, L. Østergaard, M. R. Horsman, F. Besenbacher, K. A. Howard and J. Kjems, *ACS Nano*, 2009, **3**, 1947–1951.
65 E. B. Abuin, M. A. Rubio and E. A. Lissi, *J. Colloid Interface Sci.*, 1993, **158**, 129–132.
66 T. A. S. Ferreira, J. C. Waerenborgh, M. H. R. M. Mendonça, M. R. Nunes and F. M. Costa, *Solid State Sci.*, 2003, **5**, 383–392.
67 L. Lutterotti and P. Scardi, *J. Appl. Crystallogr.*, 1990, **23**, 246–252.
68 R. A. Young and D. B. Wiles, *J. Appl. Crystallogr.*, 1982, **15**, 430–438.
69 V. Montoro, *Gazz. Chim. Ital.*, 1938, **68**, 728–733.
70 S. Mondini, A. M. Ferretti, A. Puglisi and A. Ponti, *Nanoscale*, 2012, **4**, 5356.

71 R. J. Matyi, L. H. Schwartz and J. B. Butt, *Particle Size, Particle Size Distribution, and Related Measurements of Supported Metal Catalysts*, 1987, vol. 29.
72 E. F. Kneller and F. E. Luborsky, *J. Appl. Phys.*, 1963, **34**, 656–658.
73 J. M. G. Duarte and S. L. Campbell, *Design*, 2009, **02142**, 3–7.
74 E. Murad and J. H. Johnston, *Mössbauer Spectrosc. Appl. to Inorg. Chem.*, 1987, pp. 507–583.
75 R. De Palma, S. Peeters, M. J. Van Bael, H. Van Den Rul, K. Bonroy, W. Laureyn, J. Mullens, G. Borghs and G. Maes, *Chem. Mater.*, 2007, **19**, 1821–1831.
76 S. Bandyopadhyay and A. Dey, *Analyst*, 2014, **139**, 2118–2121.
77 Z. P. Chen, Y. Zhang, S. Zhang, J. G. Xia, J. W. Liu, K. Xu and N. Gu, *Colloids Surf., A*, 2008, **316**, 210–216.
78 M. Yamaura, R. L. Camilo, L. C. Sampaio, M. A. Macêdo, M. Nakamura and H. E. Toma, *J. Magn. Magn. Mater.*, 2004, **279**, 210–217.
79 N. Shukla, C. Liu, P. M. Jones and D. Weller, *J. Magn. Magn. Mater.*, 2003, **266**, 178–184.
80 H. Zhai, Y. Wang, M. Wang, S. Liu, F. Yu, C. Gao, G. Li and Q. Wu, *Int. J. Mol. Sci.*, 2018, **19**, 3790.
81 F. Xiong, Z. Zhu, C. Xiong, X. Hua, X. Shan, Y. Zhang and N. Gu, *Pharm. Res.*, 2012, **29**, 1087–1097.
82 H. Wang, X. Zhao, W. Meng, P. Wang, F. Wu, Z. Tang, X. Han and J. P. Giesy, *Anal. Chem.*, 2015, **87**, 7667–7675.
83 Z. Tang, X. Zhao, T. Zhao, H. Wang, P. Wang, F. Wu and J. P. Giesy, *Environ. Sci. Technol.*, 2016, **50**, 8640–8648.
84 J. A. Ramos Guivar, E. A. Sanches, C. J. Magon and E. G. Ramos Fernandes, *J. Electroanal. Chem.*, 2015, **755**, 158–166.
85 S. A. Elfeky, S. E. Mahmoud and A. F. Youssef, *J. Adv. Res.*, 2017, **8**, 435–443.
86 D. Joseph, R. D. Rodriguez, A. Verma, E. Pousaneh, D. R. T. Zahn, H. Lang and S. Chandra, *RSC Adv.*, 2017, **7**, 3628–3634.
87 B. Bateer, C. Tian, Y. Qu, S. Du, Y. Yang, Z. Ren, K. Pan and H. Fu, *Dalton Trans.*, 2014, **43**, 9885–9891.
88 P. Qiu, C. Jensen, N. Charity, R. Towner and C. Mao, *J. Am. Chem. Soc.*, 2010, **132**, 17724–17732.
89 A. G. Roca, S. Veintemillas-verdaguer, M. Port, C. Robic, C. J. Serna and M. P. Morales, *J. Phys. Chem. B*, 2009, **113**, 7033–7039.
90 H. J. Kreuzer, R. L. C. Wang and M. Grunze, *J. Am. Chem. Soc.*, 2003, **125**, 8384–8389.
91 M. Kallumadil, M. Tada, T. Nakagawa, M. Abe, P. Southern and Q. a. Pankhurst, *J. Magn. Magn. Mater.*, 2009, **321**, 1509–1513.
92 I. Y. Tóth, D. Nesztor, L. Novák, E. Illés, M. Szekeres, T. Szabó and E. Tombácz, *J. Magn. Magn. Mater.*, 2017, **427**, 280–288.
93 R. S. Yadav, Anju, T. Jamatia, I. Kuřitka, J. Vilčáková, D. Škoda, P. Urbánek, M. Machovský, M. Masař, M. Urbánek, L. Kalina and J. Havlica, *Nanomaterials*, 2021, **11**, 1112.
94 V. Pilati, R. Cabreira Gomes, G. Gomide, P. Coppola, F. G. Silva, F. L. O. Paula, R. Perzynski, G. F. Goya, R. Aquino and J. Depeyrot, *J. Phys. Chem. C*, 2018, **122**, 3028–3038.
95 P. de la Presa, Y. Luengo, M. Multigner, R. Costo, M. P. Morales, G. Rivero and A. Hernando, *J. Phys. Chem. C*, 2012, **116**, 25602–25610.